The Journal of Green Energy and Environmental Engineering

Research Paper

Preparation of Floating Gel Beads and Study on Their Performance in Degrading Fluoroquinolone Antibiotics

Zahra Malfait [1,*], **Hashna Schowald** [2]

[1] Laboratory for Building Energy Materials & Components, Empa Swiss Federal Laboratories for Materials Science and Technology, Dübendorf 8600, Switzerland
[2] Department of Textile Engineering, Dhaka University of Engineering & Technology, DUET, Gazipur 1707, Bangladesh
*Corresponding author: Z.Malfait@empa.ch

Abstract. Antibiotics, as typical emerging pollutants, originated from metabolites produced by microorganisms in nature to compete for survival resources, which can inhibit or kill other microorganisms. Long-term abuse of antibiotics can lead to the rapid spread of bacterial resistance genes (ARGs) and even the emergence of "superbugs," rendering traditional antibiotics ineffective and thus posing serious environmental pollution and ecological risks. Among various treatment technologies, photocatalytic technology is a green, efficient, and highly promising method for water pollution remediation. Therefore, this study constructed a heterojunction and established a floating catalytic system to prepare photocatalytic gel beads (CA/CNF@BiOBr/Ti_3C_2) with a hollow porous structure, which simultaneously possesses favorable mass transfer properties and effective catalytic active centers. These gel beads can mineralize various fluoroquinolone antibiotics (FQs) and exhibit resistance to interference from complex water environments, along with excellent stability. The specific research results are as follows: (1) CA/CNF@BiOBr/Ti_3C_2 photo-active gel beads assembled successfully.(2) Embedding Ti_3C_2 widened the light-harvesting window and forged a BiOBr/Ti_3C_2 Schottky junction that accelerates charge parting, drives carriers outward, and trims interfacial resistance.The junction boosts the gel bead's photoelectrochemical output, turning more photons into usable current.(3) How O_2 shuttle and the self-generated electric field amplify each other inside the bead.Electrons hop from BiOBr to Ti_3C_2, sketching an internal field that tilts BiOBr's bands upward and blocks the U-turn of light-sparked electrons. On the other hand, the CA/CNF@BiOBr/Ti_3C_2 gel beads in the three-phase system can directly contact O_2 in the air and reduce its diffusion distance, thereby achieving rapid O_2 transport and sufficient supply. A steady O_2 feed devours the migrated electrons, stifling charge recombination and fueling a burst of $\cdot O_2^-$ and ·OH radicals.Ultimately, these highly oxidative ROS oxidize and decompose MOX molecules into CO_2, H_2O, and less toxic small molecules.

Keywords: *Three-phase interface; BiOBr/Ti_3C_2; Oxygen transport; Built-in electric field; Fluoroquinolone antibiotics*

Received on 03 March 2024, Accepted on 28 May 2024, Published on 15 July 2024

1 Introduction

In recent years, scientific studies have reported water pollution incidents caused by harmful antibiotics [1]. Among these, the excessive use of antibiotics is a significant factor leading to water quality deterioration, posing serious hazards toWater-based natural systems and their influence on human wellness [2].More unfortunately, antibiotic abuse may lead to the emergence of antibiotic-resistant genes (ARGs) [3] and antibiotic-resistant bacteria (ARBs) [15], triggering intricate toxic responses and emerging hazards [4]ARGs have the potential to spread from natural environmental ARBs to different bacterial strains [5], including human-related pathogens, leading to potential inadequate treatments. The proliferation and spread of ARGs and ARBs pose significant risks to public health, making it urgent to seek effective remediation strategies for antibiotic-containing wastewater [6].

Currently, the main processes for treating antibiotics in water bodies include three categories: (1) Physical adsorption; (2) Chemical oxidation (e.g., Advanced Oxidation Processes); (3) Biodegradation.

Among chemical oxidation methods [7], the most widely applied currently is the Advanced Oxidation Process (AOPs). By spawning aggressive oxidants—$\cdot OH$, $O_2\cdot^-$, $\cdot SO_4^-$ and the like [8]— AOPs dismantle antibiotic molecules with ease, earning their reputation as a green, high-speed cleanup crew for tainted water.Common AOPs used for removing antibiotics from water environments include: (1) $\cdot OH$-based AOPs, mainly including traditional Fenton and Fenton-like processes, photocatalytic oxidation, ozone (O_3)-based oxidation; (2) Persulfate activation methods based on $\cdot SO_4^-$, i.e., activating peroxymonosulfate (PMS) or peroxydisulfate (PDS) via light, heat, transition metals, or carbon-based materials; (3) Electrochemical oxidation, where pollutants are directly oxidized at the anode surface or degraded by strong oxidative radicals like ClO^- generated through electrolysis; (4) Ultrasonic oxidation, utilizing the cavitation effect of ultrasound to create local high-temperature and high-pressure environments, prompting water molecules to split into $\cdot OH$ and $H\cdot$ radicals; (5) Wet oxidation and supercritical water oxidation, among others. Among these, photocatalytic oxidation, photocatalysis, as an effective branch of AOPs, especially sunlight-driven photocatalytic systems, can utilize semiconductor photogenerated charge carriers to degrade water pollutants efficiently, environmentally friendly, and sustainably [9]. It is widely regarded as a promising and sustainable strategy for effectively eliminating antibiotics [10]. Simultaneously, photocatalytic semiconductor materials possess significant redox capabilities: photoexcited valence band holes (VB-h^+) have high oxidation potential, enabling them to activate water molecules to generate $\cdot OH$ and also directly oxidize pollutants [11]; while photoexcited conduction band electrons (CB-e^-) can reduce dissolved oxygen, producing $O_2\cdot^-$ and other reactive species (RSs) through electron transfer mechanisms [12].

The excellent photocatalytic performance of floating photocatalysts primarily benefits from their unique gas-liquid-solid three-phase interface photocatalytic system, with main advantages including: (i) rapid O_2 transport; (ii) high light utilization efficiency; (iii) convenient recovery. Molecular oxygen is indispensable to the photocatalytic pathway； sufficient O_2 can consume photogenerated electrons (e^-), further promoting the separation of photogenerated charge carriers and generating more ROS ($\cdot O_2^-$ and $\cdot OH$), thereby enhancing the catalytic activity of the photocatalyst. Classic powder catalysts work a solid–liquid boundary, sipping only the oxygen already dissolved in the broth. Yet that sparse, sluggishly diffusing reservoir chokes the redox chain and caps reaction speed.Float-and-catalysts tap air directly, trimming the trek for O_2 and parking more of it on active sites.With gaseous O_2 diffusing roughly 10^4 times faster than in water,floating rigs sweep aside the twin bottlenecks of oxygen's low solubility and sluggish aqueous crawl,feeding the three-phase boundary a steady O_2 stream that fuels lightning-fast ROS production [13]. For example, Sheng et al. [14] constructed a three-phase photocatalytic system by loading TiO_2 nanoparticles onto a superhydrophobic carbon fiber substrate. Tests show that once the reaction moves to the gas-solid-liquid junction, air-delivered O_2 instantly vacuums electrons off the catalyst face,wrenching holes and electrons apart before they can recombine. The e^-/h^+ annihilation rate in TiO_2 plunged, while ROS output in the reactor climbed sharply.leaving old two-phase setups far behind in the degradation race.

Bismuth is a particularly unique heavy metal element in nature, renowned as a "green element" due to its low toxicity and extremely low radioactivity. China is rich in bismuth resources, with explored reserves of about 240,000 tons, accounting for 75% of the world's total reserves, ranking first globally [15]. This resource advantage provides a solid foundation for the development and application of bismuth-based materials, holding significant strategic importance. In recent years, bismuth-based semiconductor materials have shown great application potential in the field of photocatalysis due to their unique physical and chemical properties, such as suitable band structure, outer electron configuration, and excellent light absorption performance. They have rapidly become a hotspot in the research of new photocatalytic materials. In bismuth-based materials, bismuth usually exists in the stable trivalent state (Bi^{3+}). Its 6s orbital hybridizes with the oxygen 2p orbital in the valence band (VB), causing the VB position to shift upward, effectively narrowing the band gap of the material and significantly enhancing the migration ability of photogenerated charge carriers [16]. This characteristic gives bismuth-based materials excellent performance in photocatalytic reactions. So far, researchers have successfully developed various bismuth-based photocatalysts, classified by chemical composition into single bismuth oxides (Bi_2O_3), bismuth-based composite oxides ($BiVO_4$, Bi_2WO_6, Bi_2MoO_6), bismuth-based sulfides (Bi_2S_3), bismuth oxyhalide compounds—BiOX where X stands for Cl, Br, or I—among others. These materials, due to their diverse structures and properties, show broad application prospects in photocatalytic pollutant degradation, water splitting for hydrogen production, and CO_2 reduction [17].

Lately, labs have raced to craft gas-solid-liquid frontiers that supercharge ROS output for faster contaminant wipe-out.Yet these tri-phase setups still underdeliver, hamstrung by sluggish charge divorce inside lone-crystal catalysts.Splitting light-born pairs fast is the make-or-break step that powers redox chemistry and sets the ceiling for catalyst performance.So the urgent brief: engineer floating photocatalysts that separate and shuttle charges at lightning speed—yet stay afloat and intact.thereby unlocking top-tier photocatalytic performance.Fortunately, pairing semiconductors into tailored heterojunctions has proven to yank electrons and holes apart before they reunite. thus cranking up the ROS yield of lone semiconductors.Sodium Alginate (SA) is a natural sugar-chain polymer harvested from brown seaweed， a waste stream pulled from brown algae such as kelp or Sargassum once iodine and mannitol have been stripped out.It’s basically a linear chain of two seaweed sugars—β-D-mannuronate (M blocks) and α-L-guluronate (G blocks)—hooked together by 1→4 linkages. SA scores high on body-friendly chemistry and sets into a gel at the drop of a divalent cation.and its price tag is seaweed-level low. It’s plentiful, cheap, and harmless—an ocean-grown polymer with a clean rap sheet [18-19]. Thanks to the crowded rows of –OH and $–COO^-$ decorating each repeat unit,SA readily latches onto di- or trivalent metal ions through coordination,weaving itself into a 3-D mesh that traps water and cargo alike. Specifically, the G units (α-L-guluronic acid) in sodium alginate fold to form cavities, and the sodium ions on the carboxyl groups ($-COO^-$) exchange with di- or trivalent metal cations (Ca^{2+}, Ba^{2+}, Sr^{2+}, Cu^{2+}, Fe^{2+}, Fe^{3+}, Cr^{3+}, etc.), forming octahedrally coordinated alginate, i.e., the classic "egg-box" gel structure [20]. Notably, when the G unit content in SA is high, it more easily forms rigid gels with higher cross-linking density with metal cations; when the M unit proportion is higher, the formed gel has better elasticity but lower mechanical strength, making it more suitable as a sustained-release drug carrier.

In this study, a $BiOBr/Ti_3C_2$ Schottky junction was first constructed via a microwave-hydrothermal strategy. Then, the $BiOBr/Ti_3C_2$ nanopowder was loaded onto a CA/CNF organic carrier using an ion-gelation dropwise injection method, synthesizing floating CA/CNF@$BiOBr/Ti_3C_2$ gel beads with a hollow porous structure. The binding mechanisms between their components were explored. The photoelectron transfer pathway in CA/CNF@$BiOBr/Ti_3C_2$ was revealed through band structure and work function analysis. The rapid O_2 transport mechanism of the CA/CNF@$BiOBr/Ti_3C_2$ gel beads was investigated by combining aeration experiments under different gas atmospheres and FEM simulation calculations. Next, quencher tests paired with EPR spin probes were run to fingerprint the dominant oxidants in play， pinpointing how CA/CNF@$BiOBr/Ti_3C_2$ dismantles moxifloxacin under light.HPLC-MS fragments and Fukui-index mapping were then stitched together to chart the antibiotic’s step-by-step breakdown route.Toxicity of MOX and its fragments was gauged with T.E.S.T. modeling plus live E. coli plate assays.

2 Materials and methods

2.1 Preparation Process of Aerogel Beads

(1) Preparation of Ti_3C_2: Ti_3C_2 was obtained by selectively etching the Al layer from Ti_3AlC_2 using a chemical etching method.

(2) Preparation of BiOBr: BiOBr was prepared using a microwave solvothermal method.

(3) Preparation of $BiOBr/Ti_3C_2$: $BiOBr/Ti_3C_2$ was prepared using the same microwave solvothermal method.

(4) Preparation of CA and CA/CNF: CA and CA/CNF were prepared using the ion-gelation dropwise injection method.

CA/CNF@BiOBr and its Ti_3C_2 twin were made alike: for the first, 0.30 g SA (1 % w/v) and 0.09 g CNF (0.3 % w/v) were tipped into a beaker,30 mL of ultrapure water followed, and the blend was magnetically stirred at 60 °C for 3 h until everything dissolved. Once the solution cooled, 0.25 g $NaHCO_3$ was dropped in and stirred for 30 min to yield solution A.Next, 0.12 g BiOBr catalyst powder was dispersed into solution A,stirred for 2 h, then briefly sonicated to chase out bubbles, giving a smooth dispersion labeled solution B. The mix was loaded into a 5 mL syringe and dripped at 60 mL h^{-1} into 5 % w/v $CaCl_2$ plus 0.8 M HA, where beads cured for 4 h. The resulting composite gel beads, now firm, were harvested, rinsed and steered straight into the next step. CA/CNF@BiOBr beads were washed free of stray Ca^{2+} and HA with ultrapure water and ethanol, then freeze-dried for 12 h to yield buoyant, hollow, porous pellets.

CA/CNF@BiOBr/Ti_3C_2 synthesis: CA/CNF@BiOBr/Ti_3C_2 was made the same ion-gel drip way: 0.30 g SA (1 % w/v) plus 0.09 g CNF (0.3 % w/v) went into a beaker,30 mL ultrapure water followed, and the mix was magnetically stirred at 60 °C for 3 h until fully dissolved.Once cooled, 0.25 g $NaHCO_3$ was added and stirred for 30 min to give solution A. Next, 0.12 g BiOBr/Ti_3C_2 composite powder was dispersed into solution A,stirred for 2 h, then briefly sonicated to remove bubbles, yielding a smooth dispersion labeled solution B.The mix was loaded into a 5 mL syringe and dripped at 60 mL h^{-1} into 5 % w/v $CaCl_2$ plus 0.8 M HA, where beads cured for 4 h.The resulting composite gel beads, now firm, were harvested for the next step.CA/CNF@BiOBr/Ti_3C_2 beads were washed clean of stray Ca^{2+} and HA with ultrapure water and ethanol, then freeze-dried for 12 h to lock in their buoyant, hollow-porous architecture. After a thorough rinse with ultrapure water and ethanol to flush out residual Ca^{2+} and HA, the beads were freeze-dried for 12 h, yielding lightweight CA/CNF@BiOBr/Ti_3C_2 pellets riddled with hollow pores that float like tiny sponges.

2.2 Aeration Experiments under Different Gas Atmospheres

The photocatalytic performance of the CA/CNF@BiOBr/Ti_3C_2 gel beads was tested using MOX as the target pollutant under different gas compositions (O_2, Air, and Ar). 0.12 g of CA/CNF@BiOBr/Ti_3C_2 gel beads were dispersed into 50 mL of a pre-prepared MOX pollutant solution (10 mg·L^{-1}, pH=6.8) in a transparent acrylic container. This container had two inlet ports on the sides and one exhaust port on the top. Different gases (O_2, Air, Ar) were introduced into the container via peristaltic pumps for aeration and exhaust to create different liquid/gas phase atmospheres. The vial was then left in the dark for 30 min to let sorption settle at equilibrium.AOnce the dark step ended, the Xe lamp—fitted with an AM 1.5G 400–780 nm filter and a PLS-LA320A homogenizer—was switched on.the reactor lid was sealed and a 120-min illumination period began.Timed sampling was performed during illumination, with 2 mL of supernatant extracted using a 5 mL PTFE syringe at time points of 20, 40, 60, 80, and 120 minutes for testing.

2.3 Finite Element Simulation

Finite Element Method (FEM) simulation was used to calculate the O_2 concentration distribution and diffusion flux around the CA/CNF@BiOBr/Ti_3C_2 gel beads in three-phase and two-phase systems. SEM shots show a hollow, shell-like bead 1 mm across with a 0.1 mm wall laced by open pores， built as a 3-D hollow sphere.This bead was then dropped into both gas-solid-liquid and liquid-solid-liquid setups for further tests.At room temp and 1 atm, the O_2 level on both bead faces was pinned at the air-saturation limit—0.26 mM.and the bead’s O_2 burn rate was fixed at 5 mM s^{-1}.

2.4 Active Species Trapping Experiments

Under the same experimental methods and conditions, 0.025 mmol of BQ (p-benzoquinone) was added to the initial MOX solution to trap $\cdot O_2^-$, while $\cdot OH$, e^-, and h^+ were trapped by adding 0.05 mmol of IPA (isopropanol), $Na_2S_2O_3$, and $Na_2C_2O_4$ (sodium oxalate), respectively, to pinpoint the key reactive intermediates driving the photocatalytic breakdown of MOX within the CA/CNF@BiOBr/Ti_3C_2 system.

To further verify the types of active species generated during the photocatalytic reaction of CA/CNF@BiOBr/Ti_3C_2, the EPR signal intensities of $\cdot O_2^-$ and $\cdot OH$ produced by the series of samples in three-phase and two-phase systems were detected using an Electron Paramagnetic Resonance spectrometer.

2.5 Pollutant Active Site Prediction

The Hirshfeld charges and condensed Fukui function of MOX were calculated using Gaussian 16W. MOX geometry was refined via B3LYP/6-31G(d) calculations.Fukui indices and electrostatic maps for MOX were generated with Multiwfn 3.8.

2.6 Intermediate Product Identification and Biotoxicity Assessment

(1) Intermediate tracking: Under CA/CNF@BiOBr/Ti_3C_2 light, MOX fractures along a traceable chain.Aliquots (2 mL) were pulled at 20, 40, 60, 80, 120 min and cleared through 0.22 µm PTFE filters; meanwhile,an untouched MOX solution was processed identically as a blank. Every vial was then diluted 10-fold with water,and 3 mL of the dilute was placed in amber vials. Xcalibur software decoded the spectra, assigning structures to the MOX fragments formed under light.Toxicity screens—96 h LC_{50} for fathead minnow, bioconcentration potential, developmental hazard—were added to round out the risk picture.Mutagenicity and related endpoints were forecast with the T.E.S.T. platform, tapping QSAR models to translate structures into probable toxic outcomes.(2) Microbe test: E. coli served as the sentinel, raised on LB broth/plates (10 g L^{-1} each of tryptone, yeast, agar and NaCl).Stepwise protocol: Strain wake-up:The glycerol stock was thawed in a 40 °C bath for 2 h to revive cells. A 100 µL aliquot of revived cells was streaked on LB agar and grown 24 h at 35 °C in the dark. Next, a single colony was dropped into LB broth and shaken at 35 °C for 12 h to reach log phase. Gradient Dilution: The bacterial culture after 12 hours was serially diluted to obtain suspensions with concentrations of 10^{-1} to 10^{-10}. Inoculation: First, 100 µL of the reaction solution (MOX pollutant solution after photocatalytic treatment by the series of samples) was pipetted onto a solid plate and air-dried. Then, 50 µL of the diluted bacterial suspension was inoculated onto the dried plate and placed in a 35°C constant temperature incubator for 24 hours in the dark. Two parallel samples were set for each test. Counting: The growth on each plate was compared, and the colony count was calculated based on the dilution factor and spreading volume.

3 Results and discussion

3.1 Analysis of Photoelectron Transfer Pathway Mechanism

High-res XPS, calibrated to the C 1s C-C line at 284.8 eV, was used to map surface chemistry and electron flow across the series.In Fig. 1a, BiOBr's Bi 4f envelope shows Bi^{3+} doublet at 159.6/165.0 eV ($4f_7/_2/4f_5/_2$) and metallic Bi at 158.6/164.2 eV. After loading BiOBr onto CA/CNF, the Bi 4f fine spectrum of CA/CNF@BiOBr showed the two characteristic peaks of Bi^{3+}: Bi $4f_7/_2$ (159.2 eV) and Bi $4f_5/_2$ (164.6 eV), which shifted by 0.6 eV towards lower binding energy compared to pure BiOBr. This is mainly attributed to the electron-rich groups (-OH and -COOH) in CA/CNF possibly donating electrons to BiOBr, increasing the electron density around Bi^{3+}, thereby reducing the binding energy of the Bi 4f orbitals. This proves the existence of interaction between BiOBr and CA/CNF, which is beneficial for the loading stability of BiOBr on CA/CNF [12]. Meanwhile, the metallic Bi signature vanished in CA/CNF@BiOBr, likely buried under the CA/CNF organic blanket. In CA/CNF@BiOBr/Ti_3C_2 the Bi 4f lines shift +0.2 eV, revealing Ti_3C_2 drains electron density from BiOBr and confirming the BiOBr → Ti_3C_2 electron drift.Br $3d_5/_2$ and Br $3d_3/_2$ in CA/CNF@BiOBr slide 0.5 eV lower than in bare BiOBr (68.2 vs 68.7 eV and 69.2 vs 69.7 eV), reinforcing the intimate contact between BiOBr and the CA/CNF matrix (Fig. 1a).A further +0.1 eV nudge in the Br 3d peaks of CA/CNF@BiOBr/Ti_3C_2 relative to CA/CNF@BiOBr signals additional electronic re-balancing once Ti_3C_2 enters the scene.The paired energy jumps—Bi 4f up, Br 3d up—seal the verdict: electrons march from BiOBr toward Ti_3C_2, cementing the BiOBr/Ti_3C_2 Schottky contact.

To trace how charges travel across the BiOBr/Ti_3C_2 Schottky gate, Mott-Schottky plots and UPS spectra were used to map the band lineup inside CA/CNF@BiOBr/Ti_3C_2. Figure 1b shows a positive M-S slope for BiOBr, branding it a classic n-type material.Extrapolating the three-frequency tangents (0.5, 1.0, 1.5 kHz) gives a flat-band potential of −0.56 V vs Ag/AgCl.Shifting to the NHE scale (E{fb, NHE} = E{fb, Ag/AgCl} + 0.2 V) yields −0.36 V [17]. For n-type solids the conduction band sits ~0.1 V below the flat-band value, pinning BiOBr's E_CB at −0.46 V [18]. Using E_VB = E_CB + E_g with E_g = 2.78 eV, BiOBr's valence band edge lands at +2.34 V.

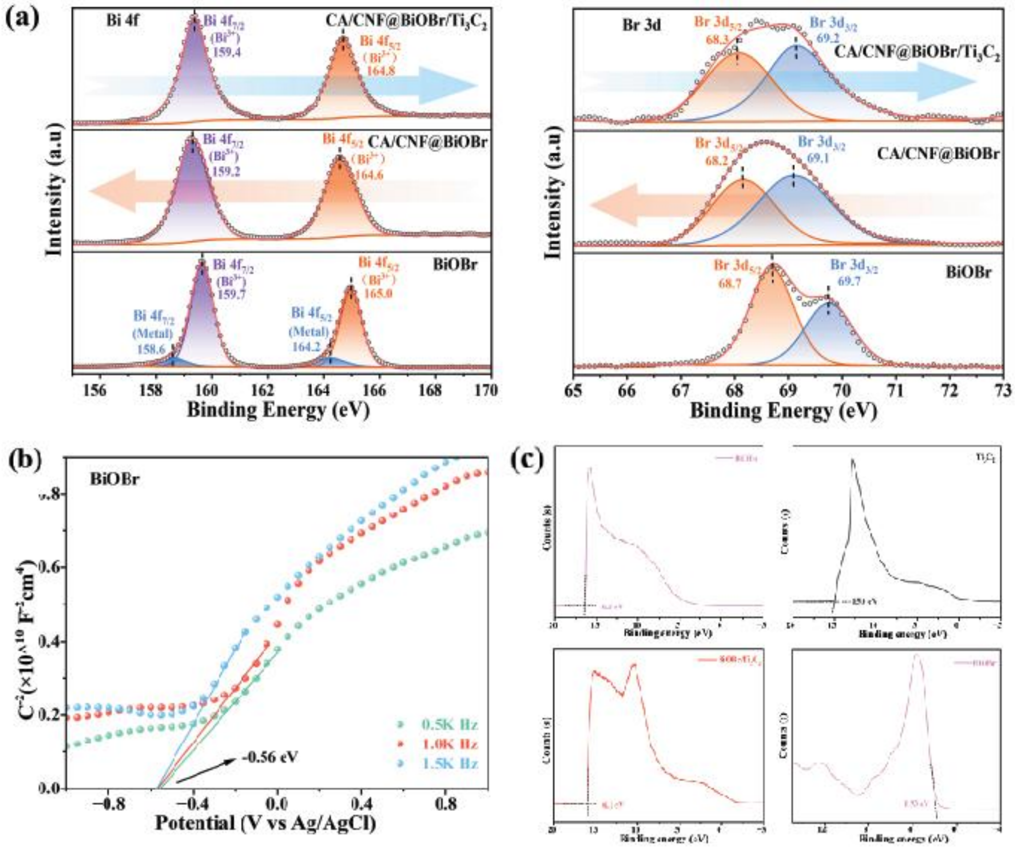

Figure 1 High-resolution XPS spectra of Bi 4f andBr 3d for CA/CNF@BiOBr/Ti3C2 (a)； Mott-Schottky plot of BiOBr (0.5k、1.0k and 1.5K Hz) (b); The UPS spectra of BiOBr, Ti3C2, BiOBr/Ti3C2, The VB-XPS of BiOBr (c)

The work function (Φ) is likewise pivotal for decoding electron traffic across heterojunction borders.Figure 1c traces the UPS cut-off edges: E_cut-off slides from 16.5 eV for BiOBr to 15.0 eV for Ti_3C_2 and 16.1 eV for the BiOBr/Ti_3C_2 blend.Plugging these into Φ = hν − E_cut-off (hν = 21.22 eV) gives work functions of 4.82, 6.22 and 5.12 eV for BiOBr, Ti_3C_2 and their junction, respectively [19].Therefore, the Fermi levels (E_F) relative to the vacuum level (E_VAC) for BiOBr, Ti_3C_2, and BiOBr/Ti_3C_2 are -4.82 eV, -6.22 eV, and -5.12 eV, respectively. Additionally, the energy gap between E_F and E_VB for BiOBr measured by VB-XPS was 1.93 eV (Figure 1d). Using the formula E_NHE (V) = E_VS (eV) - 4.44, where E_NHE and E_VS represent the energy relative to the normal hydrogen electrode and the vacuum level, respectively, the E_VB of BiOBr was calculated to be +2.31 eV. This figure aligns closely with the 2.34 eV derived from the Mott–Schottky analysis and band-gap data, matching values documented in prior studies [20]. so E_VB = 2.31 eV was used for subsequent analysis. The above analysis reveals that BiOBr and Ti_3C_2 exhibit a staggered band alignment, providing a theoretical basis for constructing a Schottky junction. Figure 1e sketches the outcome: upon contact, electrons flow from BiOBr's higher Fermi level (−4.82 eV) to Ti_3C_2's lower one (−6.22 eV), erecting an internal field pointing BiOBr → Ti_3C_2.This upward bend carves out a BiOBr/Ti_3C_2 Schottky barrier; with Φ_SBH = Φ_metal − χ the height is 0.87 eV—the lowest rung an electron must clear to jump from BiOBr's conduction band into Ti_3C_2.Φ_metal is the energy needed to transfer an electron from the metal's Fermi level into vacuum. Meanwhile, χ denotes the semiconductor's electron affinity—the energy gained when an electron drops from vacuum to the conduction-band minimum of the semiconductor [21].The Schottky junction created at the BiOBr–Ti_3C_2 boundary efficiently suppresses the recombination of light-induced electron–hole pairs.This suppression boosts the material's photocatalytic efficiency.

3.2 Active Species Enhancement Mechanism Analysis

Radical-quenching tests were first carried out to identify the dominant reactive species responsible for MOX degradation over CA/CNF@BiOBr/Ti_3C_2 under illumination.As illustrated in Figure 2a, when CA/CNF@BiOBr/Ti_3C_2 functions within a biphasic environment,introducing BQ (p-benzoquinone, a $\cdot O_2^-$ scavenger) produced the sharpest drop in degradation efficiency, whereas IPA (isopropanol, an ·OH quencher) yielded a smaller yet notable suppression.$Na_2S_2O_3$ (electron scavenger) and $Na_2C_2O_4$ (hole scavenger) produced the smallest reductions. This proves that the primary active species in the diphase photocatalytic system are $\cdot O_2^-$, followed by ·OH, e^-, and h^+. For CA/CNF@BiOBr/Ti_3C_2 operating in a triphase system, $\cdot O_2^-$ and e^- had the most significant impact on the overall reaction, followed by ·OH and h^+ (Figure 2b). Comparison revealed that after introducing BQ to trap $\cdot O_2^-$ in the photocatalytic system, the inhibition effect on CA/CNF@BiOBr/Ti_3C_2 in the triphase system (68.4%) was significantly higher than that in the diphase system (36.3%) (Figure 2c). This is mainly because the upper surface of CA/CNF@BiOBr/Ti_3C_2 in the triphase system can directly contact the abundant O_2 in the air, increasing the contact between its surface active sites and O_2 and generating more highly oxidative $\cdot O_2^-$. When these $\cdot O_2^-$ are trapped, the ROS in the system decrease significantly, thereby affecting the overall photocatalytic degradation efficiency. Furthermore, the contributions of ·OH and h^+ in the trapping experiments were different between the triphase and diphase photocatalytic systems, proving that ·OH is only partially generated by the oxidation of h^+, and the remaining ·OH may originate from the conversion of $\cdot O_2^-$.

EPR spectroscopy was then employed to track $\cdot O_2^-$ and ·OH generation by CA/CNF@BiOBr/Ti_3C_2 in both three-phase and two-phase setups.In the absence of light, neither DMPO-$\cdot O_2^-$ nor DMPO-·OH adducts were detected, confirming that radicals are not formed in the dark (Figure 2d, e).After 5 min of illumination, the 1:1:1:1 quartet characteristic of DMPO-$\cdot O_2^-$ appeared in all three samples—triphase-CA/CNF@BiOBr, diphase-CA/CNF@BiOBr/Ti_3C_2, and triphase-CA/CNF@BiOBr/Ti_3C_2 (Figure 2d).confirming $\cdot O_2^-$ production. The triphase-CA/CNF@BiOBr/Ti_3C_2 spectrum exhibited a markedly stronger DMPO-$\cdot O_2^-$ signal than triphase-CA/CNF@BiOBr,an effect ascribed to the BiOBr/Ti_3C_2 heterojunction that accelerates separation of the photogenerated charges.thereby boosting the system's capacity to generate $\cdot O_2^-$ [22]. Simultaneously, the DMPO-$\cdot O_2^-$ signal intensity for the triphase-CA/CNF@BiOBr/Ti_3C_2 photocatalytic system was also significantly higher than that for the diphase-CA/CNF@BiOBr/Ti_3C_2 system, indicating that the triphase photocatalytic system is conducive to generating more $\cdot O_2^-$. Likewise, Figure 2e reveals that triphase-CA/CNF@BiOBr, diphase-CA/CNF@BiOBr/Ti_3C_2,together with triphase-CA/CNF@BiOBr/Ti_3C_2, all displayed the 1:2:2:1 quartet fingerprint of DMPO-·OH. The DMPO-·OH peak for triphase-CA/CNF@BiOBr/Ti_3C_2 was markedly stronger than those recorded for either diphase-CA/CNF@BiOBr/Ti_3C_2 or triphase-CA/CNF@BiOBr. This is mainly because the side of CA/CNF@BiOBr/Ti_3C_2 exposed to the air in the triphase system can directly contact and utilize O_2 from the air, reducing it to generate a large amount of $\cdot O_2^-$. Meanwhile, the abundant O_2 in the air can consume photogenerated e^-, reducing e^-/h^+ pair recombination, thus favoring the generation of more ·OH. Furthermore, The signal strengths of DMPO-$\cdot O_2^-$ and DMPO-·OH progressively intensified as the illumination period extended from 0 to 5 and then to 10 min. proving that longer irradiation time helps generate more $\cdot O_2^-$ and ·OH. These results demonstrate that the construction of the BiOBr/Ti_3C_2 heterojunction and the triphase photocatalytic system contribute to the generation of more ROS ($\cdot O_2^-$ and ·OH).

From the foregoing analysis of photo-induced electron transport,a synergistic mechanism is proposed (Figure 2f) that couples accelerated O_2 supply, optimized charge-transfer channels, and reinforced radical generation to account for the superior photocatalytic activity of floating CA/CNF@BiOBr/Ti_3C_2 gel beads. Upon visible-light excitation, BiOBr electrons are promoted from the valence to the conduction band, producing abundant e^-/h^+ pairs. Upon visible-light excitation, BiOBr electrons are promoted from the valence to the conduction band, producing abundant e^-/h^+ pairs. The photoexcited electrons preferentially migrate from the BiOBr conduction band into Ti_3C_2.This charge redistribution establishes an internal electric field (IEF) pointing from BiOBr toward Ti_3C_2 and simultaneously forms a BiOBr/Ti_3C_2 Schottky barrier at their interface.The Schottky junction efficiently suppresses electron–hole recombination, and because BiOBr's conduction-band edge (-0.49 V) lies above the $O_2/\cdot O_2^-$ potential (-0.33 V), CB electrons can reduce dissolved O_2 to superoxide radicals.Likewise, the valence-band holes (+2.31 V) can oxidize OH^- to ·OH, whose potential is +1.99 V.The hollow, highly porous architecture of the CA/CNF@BiOBr/Ti_3C_2 beads shortens O_2 diffusion paths, accelerates its delivery, and enlarges the interfacial area accessible to both O_2 and the catalytically active surface.This O_2-rich micro-environment rapidly consumes photo-excited electrons, further suppressing e^-/h^+ recombination.Ultimately, the strongly oxidizing

ROS ($\cdot O_2^-$ and $\cdot OH$) produced attack and mineralize the organic pollutants.

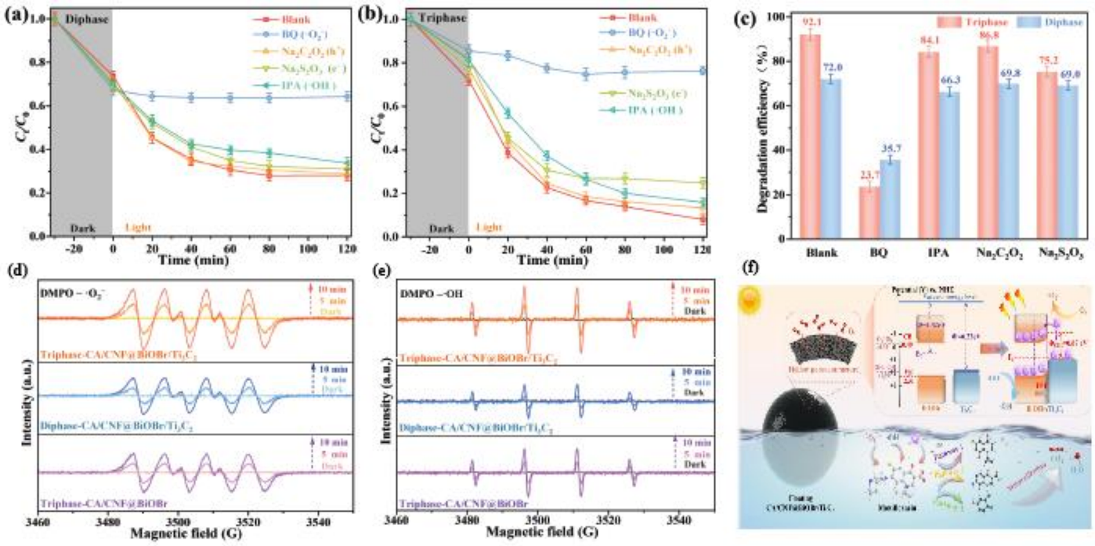

Figure 2 Quenching experiments of active species during the photocatalytic degradation of MOX byCA/CNF@BiOBr/Ti3C2 in triphase (a), diphase (b) systems and comparison (c); EPR signals for DMPO−·O2− (d)and DMPO−·OH (e) over as-prepared catalyst in different photocatalytic systems; The schematic mechanism over CA/CNF@BiOBr/Ti3C2 for efficient MOX degradation (f)

3.3 Intermediate Product Toxicity Analysis

Potential ecotoxicity of MOX and its photocatalytic by-products—expressed as 96-h LC_{50}, bioconcentration factor, developmental toxicity, and mutagenicity—was predicted with the Toxicity Estimation Software Tool (T.E.S.T.) integrated with QSAR modelling. Here, LC_{50}-96h is the median lethal concentration for fathead minnows over 96 hours, with higher values indicating lower toxicity. As shown in Figure 3a, except for intermediate B2, the LC_{50}-96h values of most MOX intermediates are higher than that of MOX itself (0.18 $mg\cdot L^{-1}$), indicating that the toxicity of most photocatalytic degradation intermediates of MOX to fathead minnows is lower than that of MOX. The bioconcentration factor reflects the accumulation capacity of a compound in organisms; a higher value indicates a greater risk of accumulation in organisms [23]. Compared to MOX, the bioconcentration factor values of most intermediates decreased, except for B2 and B4, indicating a reduced risk of accumulation of these intermediates in organisms (Figure 3b). Additionally, developmental toxicity represents the negative impact of a compound on the growth and development of organisms, while mutagenicity represents the ability of a compound to cause gene mutations. The developmental toxicity and mutagenicity indices of most intermediates were lower than those of MOX, indicating that the hazards of these intermediates to biological development and genetic stability are less than those of MOX (Figure 3c-d). The above results indicate that CA/CNF@BiOBr/Ti_3C_2 can not only efficiently degrade MOX but also significantly reduce its ecological toxicity, showing potential for environmental remediation applications.

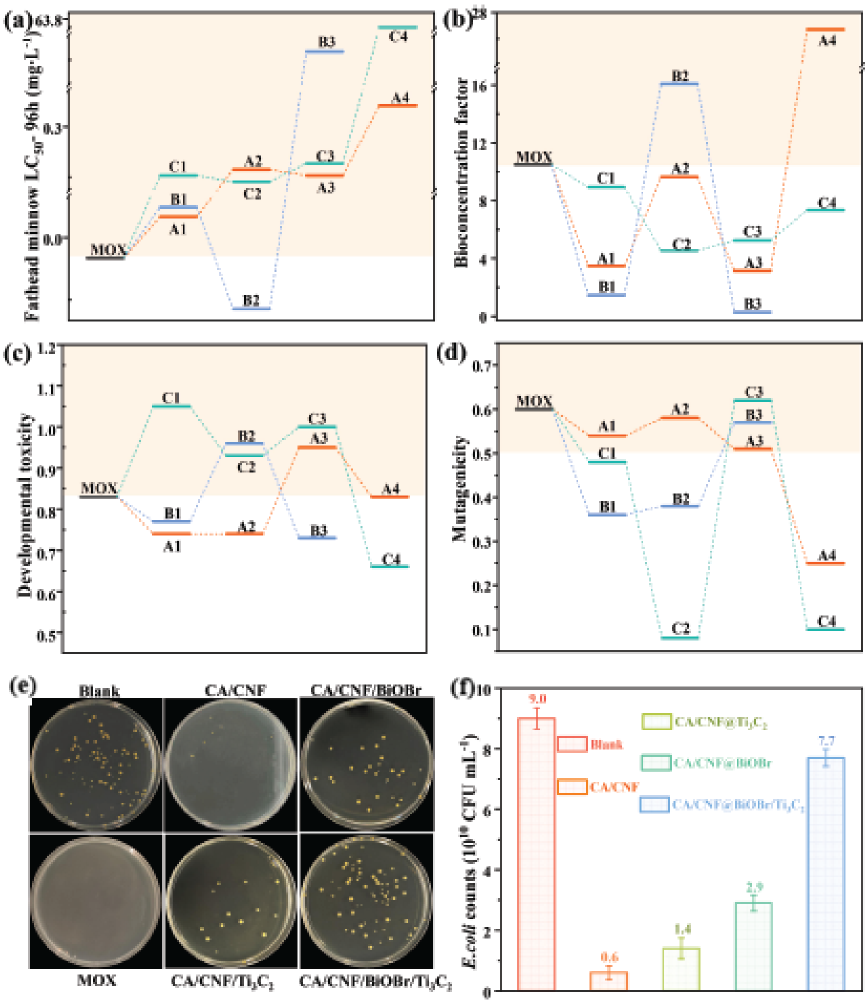

Figure 3 Fig.3 (a) Acute toxicity LC50-96 h of fathead minnow; (b) bioaccumulation factor; (c) developmental toxicity and (d) mutagenicity of MOX and intermediates; (d) Spread plate results of E. coli. treated with reaction solution by catalysts; (e) The corresponding colony counting of E.coli

The biotoxicity of MOX and its photocatalytic degradation intermediates was further evaluated using bacterial culture experiments with E. colias the representative organism. As shown in Figure 3e, E. coligrew luxuriantly and colonies were dense on the LB plate of the blank control group. No colonies appeared on the plate exposed to MOX, confirming that the antibiotic totally suppressed E. coli proliferation.an effect ascribed to MOX's antibiotic action that disrupts DNA replication and protein synthesis in bacteria. Likewise, plates inoculated with MOX solutions previously treated photocatalytically by CA/CNF, CA/CNF@Ti_3C_2, or CA/CNF@BiOBr showed colony countsof 0.6 × 10^{10}, 1.4 × 10^{10}, 2.9 × 10^{10} and 7.7 × 10^{10} CFU mL^{-1} for CA/CNF, CA/CNF@Ti_3C_2, CA/CNF@BiOBr and CA/CNF@BiOBr/Ti_3C_2, respectively (Figure 3f).The most robust E. coli growth occurred on the plate containing MOX previously degraded by CA/CNF@BiOBr/Ti_3C_2,demonstrating that CA/CNF@BiOBr/Ti_3C_2 photocatalysis markedly lowers the antibiotic's residual toxicity.thereby greatly diminishing the suppressive impact of the degradation intermediates on *E. coli*.These findings confirm that CA/CNF@BiOBr/Ti_3C_2 not only decomposes MOX efficiently but also curbs its environmental hazard.

3.4 Analysis of Material Practical Application Potential

TTo gauge real-world viability, the photocatalytic activity of CA/CNF@BiOBr/Ti_3C_2 was assessed under ambient sunlight. Figure 4a shows that CA/CNF@BiOBr/Ti_3C_2 achieves practically identical MOX removal—over 92 %—whether exposed to a lab xenon lamp or to outdoor sunlight.Yet the apparent rate constant outdoors (0.033 min^{-1}) was 1.8-fold higher than the 0.018 min^{-1} measured under the xenon lamp (Figure 4b). The reason may be that the ambient temperature under outdoor sunlight (31°C) was higher than the laboratory ambient temperature (25°C), thereby accelerating the photocatalytic reaction process.

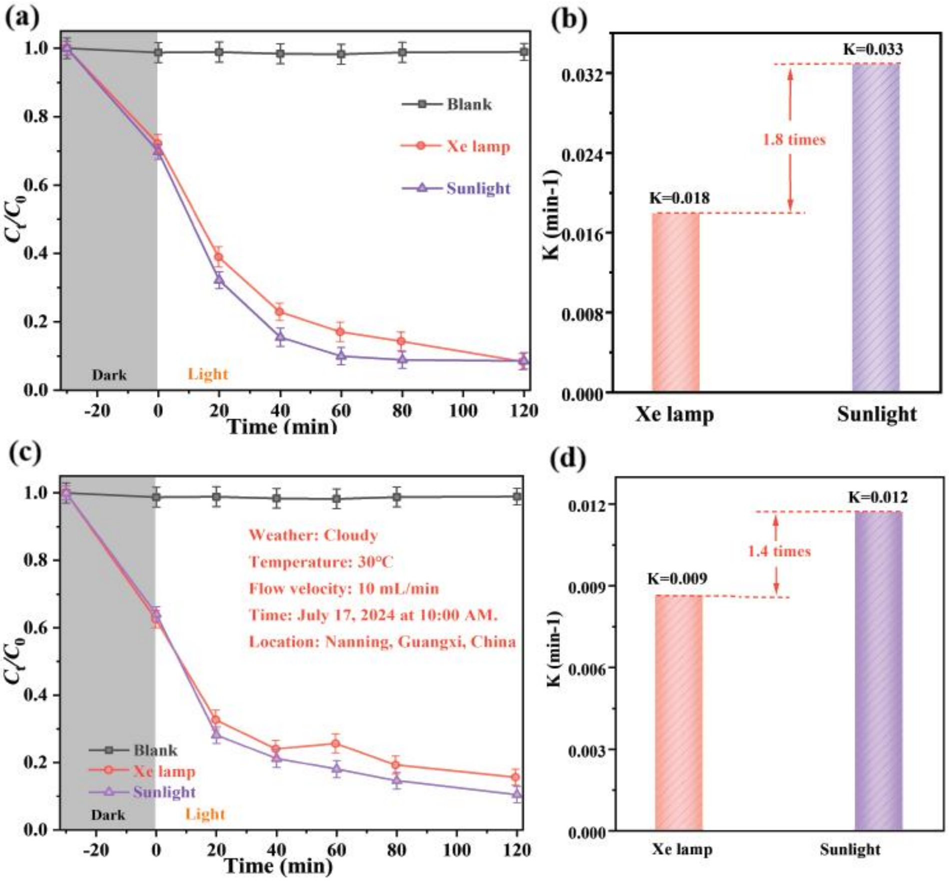

Figure 4 (a) Removal rate and (b) corresponding rate constant of MOX by CA/CNF@BiOBr/Ti3C2 under natural light conditions (The environment temperature was 31 ℃); (c) The removal rate and (d) corresponding rate constant of MOX by CA/CNF@BiOBr/Ti3C2 in a circulating flow device (MOX solution: 500 mL, catalyst: 1.2 g)

To further confirm scalability, a bench-scale recirculating reactor (500 mL MOX, 1.2 g catalyst) was employed.Figure 4c shows that, within the loop reactor, 120 min of illumination delivered 85 % MOX removal with the xenon lamp and 90 % under natural sunlight. The photocatalytic degradation rate under outdoor sunlight (0.012 min^{-1}) was 1.4 times that under laboratory xenon lamp conditions (0.009 min^{-1}). This indicates that CA/CNF@BiOBr/Ti_3C_2 has potential for large-scale application under equivalent scaling conditions.

4. Conclusion

This chapter deeply explored the mechanism of photocatalytic degradation of MOX by the floating CA/CNF@BiOBr/Ti_3C_2 gel beads from the perspectives of photoelectron transfer pathway, rapid oxygen transport mechanism, and active species enhancement mechanism, deduced the possible degradation pathway of MOX, and evaluated the biotoxicity of MOX and its degradation intermediates. The main conclusions are as follows:

The photoelectron transfer pathway of CA/CNF@BiOBr/Ti_3C_2 was clarified. High-resolution XPS combined with band structure analysis proved that the Bi 4f and Br 3d fitted peaks of CA/CNF@BiOBr/Ti_3C_2 shifted positively compared to CA/CNF@BiOBr, indicating that electrons tend to flow from BiOBr to Ti_3C_2 at the interface. This formed an internal electric field (IEF) directed from BiOBr to Ti_3C_2 at their contact interface. This further caused the conduction band (CB) of BiOBr to bend "upward," forming a BiOBr/Ti_3C_2 Schottky junction (SBH = 0.87 eV), thereby effectively inhibiting the recombination of photogenerated e^-/h^+ pairs.

The accelerated O_2-transport mechanism of the CA/CNF@BiOBr/Ti_3C_2 gel beads was elucidated.MOX removal by CA/CNF@BiOBr/Ti_3C_2 beads in the three-phase setup (92.1 %) exceeded the two-phase value (72.0 %) by 20.1 %.When CA/CNF@BiOBr/Ti_3C_2 was under gas phase conditions with O_2 (O_2/O_2, O_2/Air, O_2/Ar), its MOX removal rate and degradation rate constant were significantly higher than in other gas composition environments. This proves that the enhancement of photocatalytic performance in the triphase system mainly comes from the ample supply of gaseous O_2. Furthermore, FEM calculations proved that the O_2 diffusion flux on the upper surface of the gel bead in the triphase system was 0.151 $\mu mol\cdot(m^2\cdot s)^{-1}$ higher than in the diphase system, demonstrating that the CA/CNF@BiOBr/Ti_3C_2 gel beads in the triphase system can directly contact O_2 in the air and reduce its diffusion distance, thereby achieving rapid O_2 transport and sufficient supply.

The active species enhancement mechanism in the triphase system was elucidated. After adding BQ to scavenge $\cdot O_2^-$,the resulting drop in CA/CNF@BiOBr/Ti_3C_2 activity was far steeper in the three-phase system (68.4 %) than in the two-phase one (36.3 %).Additionally, the signal intensities of DMPO-$\cdot O_2^-$ and DMPO-$\cdot$OH for the Triphase-CA/CNF@BiOBr/Ti_3C_2 photocatalytic system were significantly higher than those for the Diphase-CA/CNF@BiOBr/Ti_3C_2 system. This is mainly attributed to the fact that CA/CNF@BiOBr/Ti_3C_2 in the triphase system can directly contact and utilize O_2 from the air, reducing it to generate a large amount of $\cdot O_2^-$, while simultaneously accelerating the consumption of photogenerated e^- and reducing the recombination rate of photogenerated charge carriers, thereby generating more $\cdot O_2^-$ and $\cdot$OH.

The breakdown route of MOX was mapped, and the toxicological risk posed by its transformation products was appraised.By coupling Fukui-function predictions with HPLC-MS data, three plausible MOX degradation routes were mapped out.Toxicity of MOX and its by-products was gauged with T.E.S.T. simulations and validated through *E. coli* viability assays,demonstrating that CA/CNF@BiOBr/Ti_3C_2 not only decomposes MOX rapidly but also markedly lessens its environmental hazard.

References

[1] LEE W, LEE C, CHA G, et al. Floatable photocatalytic hydrogel nanocomposites for large-scale solar hydrogen production[J]. Nature Nanotechnology, 2023, 18: 754–762.

[2] LIU G, YI X, CHU H, et al. Floating MIL-88A(Fe)@expanded perlites catalyst for continuous photo-Fenton degradation toward tetracyclines under artificial light and real solar light[J]. Journal of Hazardous Materials, 2024, 472: 134420.

[3] GAO X, SUN L, HAO P, et al. Construction of black g-C3N4/loofah/chitosan hydrogel as an efficient solar evaporator for desalination coupled with antibiotic degradation[J]. Separation and Purification Technology, 2025, 335: 129612

[4] ZHANG L, LI Y, LI Q, et al. Recent advances on Bismuth-based Photocatalysts: Strategies and mechanisms [J]. Chemical Engineering Journal, 2021, 419: 129484

[5] GUO J, LI X, LIANG J, et al. Fabrication and regulation of vacancy-mediated bismuth oxyhalide towards photocatalytic application: Development status and tendency[J]. Coordination Chemistry Reviews, 2021, 443: 214033.

[6] ZHANG D, WU M, HAO J, et al. Construction of Z-scheme heterojunction by coupling Bi2Sn2O7 and BiOBr with abundant oxygen vacancies: Enhanced photodegradation performance and mechanism insight[J]. Journal of Colloid and Interface Science, 2022, 612: 550–561

[7] Shi M, Li G, Li J, et al. Intrinsic facet-dependent reactivity of well-defined BiOBr nanosheets on photocatalytic water splitting[J]. Angewandte Chemie International Edition, 2020, 59(16): 6590–6595.

[8] DING J, DAI Z, QIN F, et al, Z-scheme BiO1-xBr/Bi2O2CO3 photocatalyst with rich oxygen vacancies electron mediator for highly efficient degradation of antibiotics[J]. Applied Catalysis B: Environmental, 2017, 205: 281–291.

[9] LI J, YU Y, ZHANG L. Bismuth oxyhalide nanomaterials: Laye red structures meet photocatalysis[J]. Nanoscale, 2014, 6(15): 8473–8488

[10] WEI Q, ZHOU J, AN Y, et al. Modification, 3D printing process and application of sodium alginate based hydrogels in soft tissue engineering: A review[J]. International Journal of Biological Macromolecules, 2023, 232: 123450.

[11] ZENG L, ZHE F, WANG Y, et al. Preparation of interstitial carbon doped BiOI for enhanced performance in photocatalytic nitrogen fixation and methyl orange degradation[J]. Journal of Colloid and Interface Science, 2019, 539: 563–574.

[12] VALIYATHUR M, SAKVAI M, MITHRA S, et al. Photocatalytic and toxicity assessment of alginate reinforced ZnO-g-C3N4 photocatalyst for the degradation of methylene blue – A sustainable strategy[J]. International Journal of Biological Macromolecules, 2025, 298: 139935.

[13] PENG Z, SU Y, SIAJ M. Encapsulation of tin oxide layers on gold nanoparticles decorated one-dimensional CdS nanoarrays for pure Z-scheme photoanodes towards solar hydrogen evolution[J]. Applied Catalysis B: Environmental, 2023, 330: 122614.

[14] GHIDIU M, LUKATSKAYA M R, ZHAO M Q, et al. Conductive two–dimensional titanium carbide ‘clay’ with high volumetric capacitance[J]. Nature, 2014, 516(7529): 78–81.

[15] LOW J, ZHANG T, TONG T, et al. TiO2/MXene Ti3C2 composite with excellent photocatalytic CO2 reduction activity[J]. Journal of Catalysis, 2018, 361: 255–266.

[16] TZENOV N V, BARSOUM M W. Synthesis and Characterization of Ti3AlC2[J]. Journal of the American Ceramic Society, 2000,83(4): 825–832.

[17] ZHANG Z, LUO Y, LI M, et al. A self-floating graphite felt evaporator: Interface wetting control and its application in environmental remediation and desalination[J]. Chemical Engineering Journal, 2024, 488: 151038.

[18] CHEN Y, LIU X, ZHOU R, et al. Porous sodium alginate/cellulose nanofiber composite hydrogel microspheres for heavy metal removal in wastewater[J]. International Journal of Biological Macromolecules, 2024, 278: 135000.

[19] ZHOU Y, YU M, ZHAN R, et al. Ti3C2 MXene-induced interface electron separation in g-C3N4/Ti3C2 MXene/MoSe2 Z-scheme heterojunction for enhancing visible light-irradiated enoxacin degradation[J]. Separation and Purification Technology, 2021, 275: 119194.

[20] ZHAO X F, RADOVIC M, GREEN M J. Synthesizing MXene Nanosheets by Water–free Etching[J]. Chem, 2020, 6(3): 544–546.

[21] SUBRAMANIAN Y, MARIADHAS J, MINH T, et al. Efficient degradation of methylene blue and ciprofloxacin compounds using heteroanionic titanium oxycarbide photocatalyst and its correlation with their dielectric properties[J]. Journal of Alloys and Compounds, 2024, 1004: 175906.

[22] ELSHAHAWY M, AHMED N, MOHAMED, et al. Radiation synthesis and photocatalytic performance of floated graphene oxide decorated ZnO/alginate-based beads for methylene blue degradation under visible light irradiation[J]. International Journal of Biological Macromolecules, 2023, 243: 125121.